# In vivo bioluminescence imaging of labile iron accumulation in a murine model of *Acinetobacter baumannii* infection

Allegra T. Aron[a,1], Marie C. Heffern[a,1,2], Zachery R. Lonergan[b,1], Mark N. Vander Wal[a], Brian R. Blank[c], Benjamin Spangler[c], Yaofang Zhang[d,e], Hyo Min Park[f], Andreas Stahl[f], Adam R. Renslo[c], Eric P. Skaar[b,3], and Christopher J. Chang[a,g,h,3]

[a]Department of Chemistry, University of California, Berkeley, CA 94720; [b]Department of Pathology, Microbiology, and Immunology, Vanderbilt University Medical Center, Nashville, TN 37232; [c]Department of Pharmaceutical Chemistry, University of California, San Francisco, CA 94158; [d]Mass Spectrometry Research Center, Vanderbilt University, Nashville, TN 37232; [e]Department of Biochemistry, Vanderbilt University, Nashville, TN 37232; [f]Department of Nutritional Sciences and Toxicology, University of California, Berkeley, CA 94720; [g]Department of Molecular and Cell Biology, University of California, Berkeley, CA 94720; and [h]Howard Hughes Medical Institute, University of California, Berkeley, CA 94720

Edited by Harry B. Gray, California Institute of Technology, Pasadena, CA, and approved October 26, 2017 (received for review May 26, 2017)

**Iron is an essential metal for all organisms, yet disruption of its homeostasis, particularly in labile forms that can contribute to oxidative stress, is connected to diseases ranging from infection to cancer to neurodegeneration. Iron deficiency is also among the most common nutritional deficiencies worldwide. To advance studies of iron in healthy and disease states, we now report the synthesis and characterization of iron-caged luciferin-1 (ICL-1), a bioluminescent probe that enables longitudinal monitoring of labile iron pools (LIPs) in living animals. ICL-1 utilizes a bioinspired endoperoxide trigger to release D-aminoluciferin for selective reactivity-based detection of $Fe^{2+}$ with metal and oxidation state specificity. The probe can detect physiological changes in labile $Fe^{2+}$ levels in live cells and mice experiencing iron deficiency or overload. Application of ICL-1 in a model of systemic bacterial infection reveals increased iron accumulation in infected tissues that accompany transcriptional changes consistent with elevations in both iron acquisition and retention. The ability to assess iron status in living animals provides a powerful technology for studying the contributions of iron metabolism to physiology and pathology.**

labile iron | molecular imaging | luciferin | metal homeostasis | infectious disease

Iron is an essential mineral for nearly every form of life, owing in large part to its ability to cycle between different oxidation states for processes such as nucleotide synthesis, oxygen transport, and respiration (1, 2). At the same time, the potent redox activity of iron is potentially toxic, particularly in unregulated labile forms that can trigger aberrant production of reactive oxygen species via Fenton chemistry (3). Indeed, iron deficiency remains one of the most common nutritional deficiencies in the world (4), and aberrant iron levels have been linked to various ailments, including cancer (5–7), cardiovascular (8), and neurodegenerative (9) disorders, as well as aging (10). The situation is especially complex in infectious diseases, where the requirement for iron by both host organism and invading pathogen leads to an intricate chemical tug-of-war for this metal nutrient during various stages of the immune response (11, 12).

The foregoing examples provide motivation for developing technologies to monitor biological iron status, with particular interest in methods to achieve in vivo iron imaging in live animal models that go beyond current state-of-the-art assays that are limited primarily to cell culture specimens. In this regard, detection of iron with both metal and oxidation state specificity is of central importance, because while iron is stored primarily in the ferric oxidation state, a ferrous iron pool loosely bound to cellular ligands, defined as the labile iron pool (LIP), exists at the center of highly regulated networks that control iron acquisition, trafficking, and excretion. Indeed, as a weak binder on the Irving–Williams stability series (13), $Fe^{2+}$ provides a challenge for detection by traditional recognition-based approaches (14), and as such we (15–17) and others (18–20) have pursued activity-based sensing approaches to detect labile $Fe^{2+}$ stores in cells (21–25). These tools have already provided insights into iron biology, as illustrated by the direct identification of elevations in LIPs during ferroptosis (26, 27), an emerging form of cell death, using the ratiometric iron indicator FIP-1 (15).

We now report the design, synthesis, and molecular imaging applications of iron-caged luciferin-1 (ICL-1), a first-generation caged luciferin probe that enables in vivo iron imaging in living animals. Work from our laboratory and others has demonstrated the utility of caged luciferins in vivo (28–30) for measuring transient small molecules (31–34), enzyme and transporter activities (34–46), protein–protein and cell–cell interactions (42, 47, 48), and copper (49). Indeed, previous work from our laboratory utilized a Cu-dependent oxidation reaction to uncage luciferin for in vivo copper imaging (50), a first demonstration of a general activity-based sensing (ABS) strategy which we envisioned expanding to other essential metals in biology by changing the reaction trigger.

## Significance

Iron is a required metal nutrient for life, and its altered homeostasis is associated with a number of diseases. We present a bioluminescent reporter for visualizing iron pools in living animals, where iron-dependent uncaging of D-aminoluciferin enables sensitive and selective imaging of ferrous over ferric forms of iron in luciferase-expressing cell and mouse models. Application of this technology to a model of systemic bacterial infection reveals elevation of iron in infected tissues that accompany markers for increased iron acquisition and retention. These data establish the ability to assess iron status in living animals and provide a unique platform for studying its contributions to stages of health, aging, and disease.

Author contributions: A.T.A., M.C.H., Z.R.L., M.N.V.W., A.R.R., E.P.S., and C.J.C. designed research; A.T.A., M.C.H., Z.R.L., M.N.V.W., and Y.Z. performed research; B.R.B., B.S., H.M.P., A.S., and A.R.R. contributed new reagents/analytic tools; A.T.A., M.C.H., and Z.R.L. analyzed data; and A.T.A., M.C.H., Z.R.L., and C.J.C. wrote the paper.

The authors declare no conflict of interest.

This article is a PNAS Direct Submission.

Published under the PNAS license.

[1]A.T.A., M.C.H., and Z.R.L. contributed equally to this work.

[2]Present address: Department of Chemistry, University of California, Davis, CA 95616.

[3]To whom correspondence may be addressed. Email: eric.skaar@vanderbilt.edu or chrischang@berkeley.edu.

This article contains supporting information online at www.pnas.org/lookup/suppl/doi:10.1073/pnas.1708747114/-/DCSupplemental.

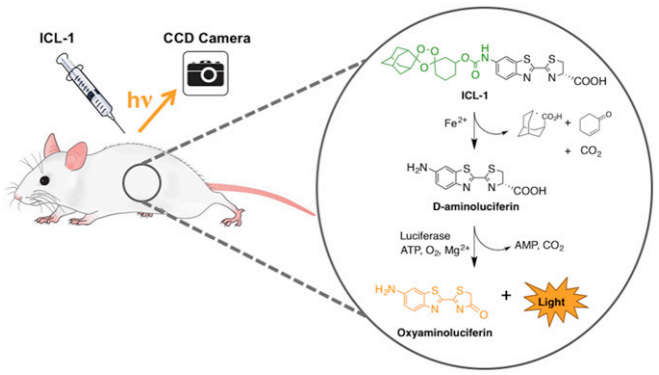


**Scheme 1.** $Fe^{2+}$-dependent cleavage of iron-caged luciferin-1 (ICL-1), an endoperoxide-luciferin conjugate and in vivo probe of $Fe^{2+}$.

In ICL-1, we caged D-aminoluciferin with an $Fe^{2+}$-reactive endoperoxide trigger (15, 17, 51) inspired by antimalarial agents that exhibit $Fe^{2+}$-dependent pharmacology (52, 53). ICL-1 was designed to undergo metal- and redox-specific $Fe^{2+}$-dependent cleavage to generate D-aminoluciferin, which can interact with the firefly luciferase enzyme to produce red light output through a catalytic bioluminescent reaction. ICL-1 is capable of monitoring changes in LIPs in live cells and mice under situations of iron overload and/or deficiency. Application of this technology to a mouse model of systemic *Acinetobacter baumannii* infection, a Gram-negative bacterial pathogen that infects susceptible intensive care unit (ICU) populations, reveals an elevation of LIPs by in vivo imaging that coregisters with increases in total iron as monitored by ex vivo imaging using laser ablation inductively coupled plasma mass spectrometry (LA–ICP-MS). This unique tool for imaging iron in living animals provides a platform for probing the contributions of this metal to physiology, aging, and disease.

## Results and Discussion

**Design and Synthesis of ICL-1.** Our design of ICL-1 involved caging D-luciferin with a 1,2,4-trioxolane scaffold (51) used previously for in vivo delivery of therapeutic payloads in an $Fe^{2+}$-dependent manner (50, 54). The excellent pharmacokinetic properties of these therapeutic conjugates suggested that ICL-1 would have suitable in vivo properties for the desired imaging applications. In the conjugate form, ICL-1 is an incompetent substrate for the luciferase enzyme. Upon $Fe^{2+}$-promoted reduction of the peroxide, however, a cyclohexanone intermediate is formed that spontaneously releases free D-aminoluciferin, which luciferase can transform to produce a bioluminescent signal (Scheme 1). D-Aminoluciferin imaging can be used as a control for changes in enzyme activity and can be used in parallel for signal normalization. Scheme 2 depicts the synthetic route to ICL-1. Briefly, commercially available 6-amino-2-cyanobenzothiazole is activated using triphosgene, which is subsequently reacted with (±)-*trans*-**1** (51) to yield carbamate **2**. Cyclization of **2** with D-cysteine-HCl affords ABS probe ICL-1 after HPLC purification.

**Reactivity and Selectivity of ICL-1.** $Fe^{2+}$-dependent reactivity of ICL-1 was assessed in aqueous solution buffered to physiological pH (50 mM Hepes, pH 7.4). Treatment of 5 μM ICL-1 with ferrous ammonium sulfate (FAS) as an $Fe^{2+}$ source at concentrations spanning 25–100 μM shows a dose-dependent increase in bioluminescent signal in the presence of luciferase (Fig. 1*A*, gray bars), saturating at a ∼7-fold bioluminescent signal enhancement at highest $Fe^{2+}$ concentrations, when incubation is performed aerobically, versus a ∼30-fold bioluminescent signal enhancement at the same $Fe^{2+}$ concentration, when incubation is performed anaerobically (*SI Appendix*, Fig. S1). The observed signal increase is $Fe^{2+}$ dependent, as coincubation of ICL-1/luciferase solutions with the $Fe^{2+}$ chelator bipyridine (BPY) results in a decrease in bioluminescence intensity (Fig. 1*A*, gray patterned bars). Further control experiments establish that iron-dependent responses are not observed with the parent D-aminoluciferin substrate (*SI Appendix*, Fig. S2), aside from a slight decrease in signal observed with hemoglobin. ICL-1 exhibits high selectivity for $Fe^{2+}$ over other biologically relevant d-block and s-block metals, including redox-active copper and cobalt transition metals (Fig. 1*B*). A modest response is observed with free copper salts, as is similarly observed for the related fluorescence probe FIP-1 (15). However, as a typical eukaryotic cell exhibits a ∼10-fold higher level of iron over copper coupled with the high buffering capacity of copper with glutathione and metallochaperones (picomolar to femtomolar $K_d$ values) (55–60), the modest response to free copper salts suggests that ICL-1 should have sufficient selectivity to detect alterations in biological ferrous iron levels. ICL-1 is also selective for labile $Fe^{2+}$ over other biologically relevant forms of iron that are tightly bound to proteins and cofactors, such as transferrin, ferritin, hemin, and hemoglobin, as well as $Fe^{3+}$, along with reductants glutathione, *N*-acetyl cysteine, β-mercaptoethanol, and ascorbic acid (Fig. 1*C*).

**ICL-1 Detects Changes in Labile Iron Levels in Living Cells.** We next sought to evaluate the ability of the ICL-1 probe to detect changes in $Fe^{2+}$ levels in live cells. Initial experiments employed a luciferase-expressing prostate cancer cell line, PC3M-luc, that has been shown previously to respond to Trx-puro (17), a cellular $Fe^{2+}$ probe based on the same caging moiety used in ICL-1. Cells were supplemented with various concentrations of an iron salt (FAS), iron chelator (BPY), or FAS followed by BPY, and then treated with ICL-1 and imaged using a CCD camera (IVIS, Xenogen) for bioluminescence (Fig. 2). Iron supplementation results in an increase in ICL-1–dependent bioluminescence that can be attenuated by addition of BPY. Additionally, iron deficiency induced by treatment with BPY alone results in a decrease in ICL-1 signal relative to basal levels. Notably, ICL-1 exhibits excellent stability in media (*SI Appendix*, Fig. S3). Additionally, ICL-1 signal is unaffected by short-term treatment with a cell-impermeable, extracellular iron chelator, bathophenanthrolinedisulfonic acid (BPS), suggesting that observed ICL-1 reactivity is due to intracellular, as opposed to extracellular, iron (*SI Appendix*, Fig. S4). Control experiments with the parent D-aminoluciferin substrate show no sensitivity to iron status.

The probe was further evaluated in a broader set of luciferase-expressing cell lines and with additional iron chelators. In addition to PC3M-luc, a second prostate cancer cell line (LNCaP-luc), breast cancer cell line (MDA-MB-231-luc), and embryonic kidney cell line (HEK293-luc) were each treated with FAS, the iron chelators desferroxamine (DFO), BPS, or BPY, or a combination of FAS and BPY for ICL-1 imaging (*SI Appendix*, Fig. S5). Consistent with what is observed using PC3M-luc cells, LNCaP-luc, MDA-MB-231-luc, and HEK-293-luc cells supplemented with 100 μM FAS exhibit increased light production relative to untreated control cells, and these increases are attenuated by coincubation with the iron chelator BPY. Likewise, iron depletion induced by chelator addition results in decreases in ICL-1–dependent bioluminescence in all cell lines tested. Again, control experiments confirm that

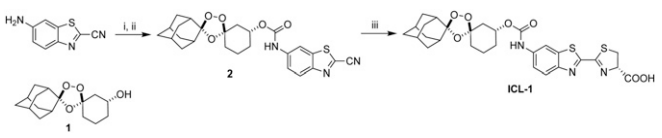


**Scheme 2.** Synthesis of ICL-1[a]. [a]Reagents and conditions: (*i*) triphosgene, 4-DMAP, toluene, 125 to 35 °C, 3 h; (*ii*) **1**, NaH, toluene, 35 °C, 12 h; and (*iii*) D-cysteine, $K_2CO_3$, $CH_2Cl_2$, MeOH, $H_2O$, 0 °C, 12 h.

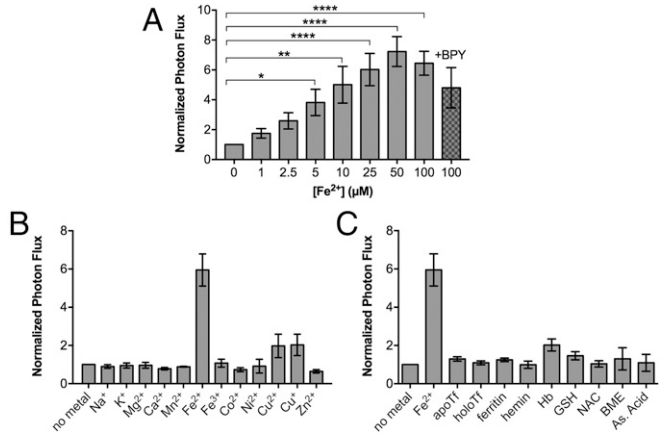


**Fig. 1.** ICL-1 responds to $Fe^{2+}$ over other metals and tightly bound biological iron species with metal and redox specificity. Bioluminescence response of ICL-1 incubated with (*A*) varying concentrations of $Fe^{2+}$ [ferrous ammonium sulfate salt (FAS)] (gray bars) or 100 μM FAS with 100 μM of bipyridine (BPY) (gray patterned bars), (*B*) various biologically relevant s-block (1 mM), d-block (100 μM) metal ions, and (*C*) tightly bound iron species of biological relevance: transferrin (without iron, apoTf; with iron, holoTf), ferritin, hemin, and hemoglobin (Hb), and reductants at 3 mM, such as glutathione (GSH), *N*-acetyl cysteine (NAC), β-mercaptoethanol (BME), and ascorbic acid (as. acid). Signals are integrated over 30 min and expressed as photon fluxes normalized to ICL-1 bioluminescence with no treatment (buffer alone). Statistical analyses were performed with one-way ANOVA with multiple comparisons to the control with no metal treatment (*$P \leq 0.05$, **$P \leq 0.01$, and ****$P \leq 0.0001$). Error bars are ±SEM ($n = 3$).

D-aminoluciferin signal is not affected by either iron supplementation and/or depletion (*SI Appendix*, Fig. S6). The data establish that ICL-1 can assess labile $Fe^{2+}$ status across many cell types.

**ICL-1 Detects Changes in Labile Iron Levels in Living Mice.** Having established the ability of ICL-1 to assess labile iron levels in living cells, we next utilized this chemical tool to visualize labile iron stores in living mice. For these studies, we employed FVB-luc$^+$ mice strains using the actin-promoter to induce expression of this enzyme in virtually all organs. The i.p. injection of varying amounts of ICL-1 (10, 25, 50, 100, and 200 nmol; *SI Appendix*, Fig. S7) into age- and weight-matched male FVB-luc$^+$ mice was performed with subsequent IVIS imaging of the live mice. The ICL-1–dependent bioluminescent signal rises with increasing probe dose in the range of 10–50 nmol, with saturation at ≥100 nmol of injected probe. The signal shows the most intense localization in the peritoneal region and is consistent with the expected high levels of iron in the intestines (Fig. 3*A*). Administration of ICL-1 into the bloodstream via retroorbital injection mirrors the signal visualized in animals with D-luciferin injected through the same route (*SI Appendix*, Fig. S8). The long-term clearance kinetics in male FVB-Luc$^+$ mice was evaluated at a dose of 25 nmol of ICL-1; the bioluminescent signal sharply increases from 0 to 20 min postinjection of the probe and slowly clears by 6 h (*SI Appendix*, Fig. S9 *A* and *C*). The clearance kinetics differs from that of D-luciferin, the native substrate of firefly luciferase, which peaks in bioluminescence at 5 min and rapidly clears by 3 h (*SI Appendix*, Fig. S9 *B* and *D*). The observed differences between the metabolic clearances of ICL-1 and D-luciferin are consistent with the slow kinetics of the trioxolane-based trigger to release the parent luciferin from ICL-1 upon reaction with $Fe^{2+}$, relative to bioluminescence generation from enzymatic recognition and clearance from the system. Interestingly, the ICL-1 probe response is different between male and female mice, with the females exhibiting a greater than twofold increase in signal over males (*SI Appendix*, Fig. S10*A*). In contrast, injection of both male and female mice with equivalent doses of D-luciferin results in similar bioluminescent signal (*SI Appendix*, Fig. S10*B*). The results suggest that females may have higher resting levels of LIPs compared with males, an interesting but complex observation that merits further investigation (61, 62).

To determine the responses of ICL-1 to elevations in iron levels, male FVB-luc$^+$ mice were treated with a sublethal dose of an iron supplement, ferric ammonium citrate (FAC), 1 h before probe injection (Fig. 3). The data are plotted as a ratio of signals from treated animals over animals under basal conditions, determined from a 25-nmol i.p. injection of ICL-1 for each corresponding animal 2–4 d before treatment with FAC. Treatment of FAC-supplemented mice with 20 mg/kg ICL-1 introduced by i.p. injection resulted in a ∼77% increase in signal over mice treated with Dulbecco's PBS (DPBS) vehicle alone. In contrast, FAC-supplemented mice that were subsequently treated with the ferrous iron chelator BPY for 20 min before probe injection (8 mg/kg, i.p.) showed a ∼47% reduction in signal compared with mice treated with vehicle alone. Further experiments establish that ICL-1 can also respond to depletion of basal levels of LIPs, with a ∼86% decrease in signal observed in mice treated with BPY (8 mg/kg, i.p.) compared with vehicle control. In line with what was observed in cell-based assays, mice treated with the same doses of either FAC or BPY and imaged with parent D-luciferin do not exhibit differences in bioluminescent signal (*SI Appendix*, Fig. S11). Taken together, the data establish the ability of ICL-1 to monitor fluctuations in the labile ferrous iron levels in living animals.

**ICL-1 Visualizes Changes in Labile Iron Pools in an *A. baumannii* Model of Systemic Infection.** To showcase how ICL-1 can enable in vivo studies of iron biology, we next utilized this reagent in a live-mouse model of bacterial infection. Indeed, host–pathogen interactions involve a competition for iron as a central resource that is essential to both host organisms and microbial pathogens (63). The vertebrate host employs immune defense mechanisms to regulate iron pools against invading pathogens, which in turn have counterstrategies to evade such defenses. As a starting point, we turned our attention to *A. baumannii*, a Gram-negative

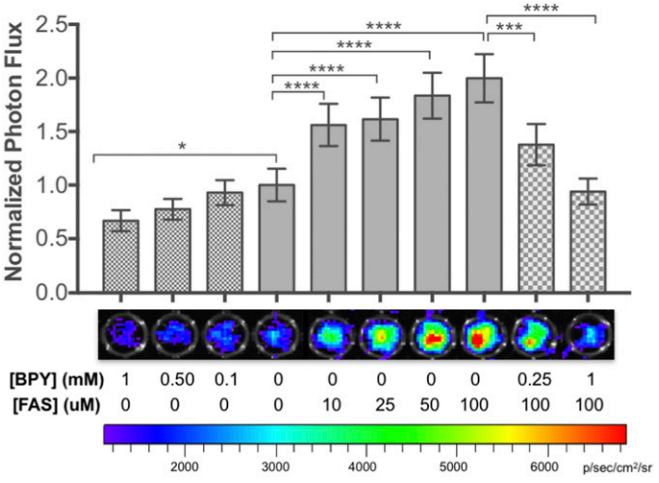


**Fig. 2.** Bioluminescent signals from PC3M-luc cells probed with ICL-1. Cells were supplemented with FAS for 90 min, BPY for 30 min, or a combination the two chemicals followed by addition of ICL-1 (20 μM). Total photon flux was integrated over 1 h and normalized to cells treated with buffer alone. Representative images of PC3M-luc cells with each treatment are shown below the corresponding data bar in the graph. Statistical analyses were performed with one-way ANOVA with multiple comparisons to the control with no metal treatment (*$P \leq 0.05$, ***$P \leq 0.001$, and ****$P \leq 0.0001$). Error bars are ±SD ($n = 3$–5).

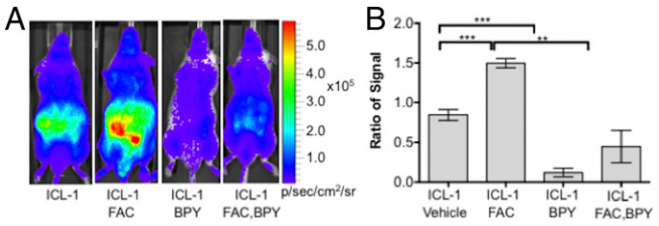


**Fig. 3.** ICL-1 monitors labile iron dynamics in luciferase-expressing mice. FVB-luc$^+$ mice were injected (i.p.) with ICL-1 (25 nmol) after i.p. injection of vehicle (DPBS), FAC (20 mg/kg), BPY (8 mg/kg), or both FAC and BPY. Mice were injected with vehicle or FAC 1 h before injection of ICL-1 and with BPY 20 min before injection of ICL-1. (*A*) Representative images of FVB-luc$^+$ mice treated with vehicle, FAC, and/or BPY and imaged with ICL-1. (*B*) Ratios of the total photon fluxes from ICL-1 of treated animals to their basal signals. Bioluminescent photon fluxes were acquired 0–50 min postinjection of the ICL-1 (i.p. injection, 25 nmol). Statistical analyses were performed with a two-tailed Student's *t* test (***P* ≤ 0.01 and ****P* ≤ 0.001). Error bars are ±SEM (*n* = 3–7).

bacterium that frequently infects patients with impaired immune systems, such as those found in hospitals (ICUs), making it a significant health care risk with rises in antibiotic resistance. In this regard, although the precise mechanisms that govern metal nutrient starvation by the host during *A. baumannii* infection remain elusive, previous work has established the importance of iron for its growth in vertebrates. Moreover, adaptations have been identified in the pathogen pointing to the development of iron-dependent survival responses, including up-regulation of the ferric uptake regulator (Fur) and its regulon during nutrient iron starvation.

Given the importance of iron regulation to *A. baumannii*, we utilized ICL-1 to assess alterations in iron status in living mice infected with this pathogen. Male FVB-luc$^+$ mice were systemically infected with wild-type *A. baumannii* ($2.0 \times 10^8$ to $4.0 \times 10^8$ CFUs) or with mock treatments (PBS; termed "mock-infected") through retroorbital injection and imaged with ICL-1 with an IVIS imager 24 h postinoculation (Fig. 4*A*). Following the in vivo imaging experiments, the lungs, hearts, kidneys, and livers of the mice were harvested and homogenized, and the bacterial burdens were enumerated. The inoculated mice confirmed detectable levels of infection in all organs tested, consistent with sepsis (Fig. 4*B*). Compared with mock-infected mice, the *A. baumannii*-infected mice displayed notable elevations in total bioluminescence signal from ICL-1 (Fig. 4*A* and *SI Appendix*, Fig. S12*A*). Importantly, such differences between mock and infected cohorts were not evident in mice that were imaged with D-luciferin that is not iron-responsive (*SI Appendix*, Fig. S12*B*). Moreover, we observed a patent difference in the iron-dependent localization of ICL-1 bioluminescence signal in infected versus mock-infected mice. The highest signal intensities in the mock-infected mice are localized to peritoneal region, whereas the ICL-1 bioluminescent signal in the infected mice is localized to the upper dorsal regions of the animals, which contain the heart, lung, and liver (Fig. 4*A*). This infection-dependent signal increase was further validated with ex vivo bioluminescent imaging after ICL-1 administration (*SI Appendix*, Fig. S13). Furthermore, the degree of bacterial burden in the lungs, hearts, and livers of the individual mice largely track with the observed localization of ICL-1 signal in each corresponding mouse (*SI Appendix*, Fig. S14). In contrast, while some slight relocalization in signal was observed in infected mice imaged with D-luciferin (*SI Appendix*, Fig. S15), possibly due to ATP release or altered respiration in infected tissues, the changes were to a far lesser degree than in the infected mice imaged with ICL-1.

Having observed the differences in labile iron stores between mice infected with *A. baumannii* compared with mock controls, we next performed ex vivo metal analyses on the tissues of the

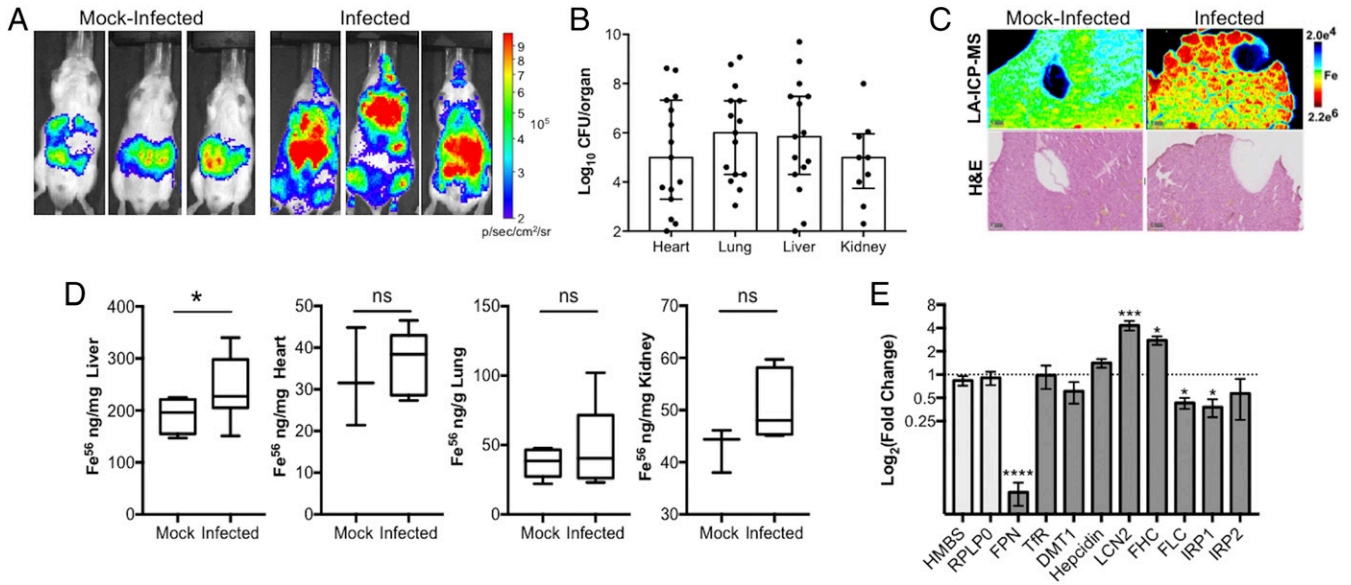


**Fig. 4.** ICL-1 imaging visualizes changes in tissue labile iron levels and distributions in systemic infection with *A. baumannii*. (*A*) Representative images of FVB-Luc$^+$ mice mock-infected (PBS) or infected with *A. baumannii* through retroorbital injection (dorsal images at 30 min postinjection of ICL-1) and imaged with ICL-1 (25 nmol) at 24 h postinfection. (*B*) Bacterial burdens in the organs of infected mice represented as scatter plots; bars represent the medians, with each organ being significantly colonized (*P* ≤ 0.005, Wilcoxon signed rank test). Error bars are interquartile ranges (*n* = 9–15). (*C*) LA–ICP-MS analysis of iron in liver tissue slices from a mock-infected and an infected mouse (*Top*) and H&E stains of the corresponding slices (*Bottom*). (*D*) Liquid ICP-MS analysis of total iron in organs of mock-infected and infected mice (24 h postinfection). Data are represented as box-and-whiskers plots (*n* = 3–9). Statistical analyses were performed with a two-tailed Student's *t* test (**P* ≤ 0.05). (*E*) Gene expression analysis of iron proteins in homogenized liver tissues by real-time PCR; mRNA levels are normalized to GAPDH. Data are plotted as the $\log_2$ fold change of the mean gene expression in the livers of infected mice from those of mock-infected mice. Ferroportin (FPN), transferrin receptor (TfR), divalent metal transporter-1 (DMT-1), hepcidin, lipocalin-2 (LCN2), ferritin heavy chain (FHC) and light chain (FLC), and regulatory proteins IRP1 and IRP2 (dark gray bars) were evaluated. Additional housekeeping genes (HMBS and RLPL0) are included as controls (light gray bars). Statistical analyses were performed on $\Delta\Delta C_t$ values with one-way ANOVA with multiple comparisons to the GAPDH control (**P* ≤ 0.05, ****P* ≤ 0.001, and *****P* ≤ 0.0001). Error bars are ±SEM (*n* = 4–6).

infected mice to directly measure and coregister total iron status. First, to assess whether the changes in ICL-1 signal could be attributed to changes in total iron in the tissues, we performed bulk inductively coupled plasma mass spectrometry (ICP-MS) on the lung, liver, heart, and kidney. Whereas no statistically significant differences in total iron levels were observed in the heart, lung, and kidney, a statistically significant elevation of total iron levels was observed specifically in livers of infected mice (Fig. 4*D*). Such elevations were further corroborated by elemental analysis of iron distributions in liver sections by LA–ICP-MS. As shown in Fig. 4*C*, regions of elevated iron were observed in the peripheries of the liver slices of infected mice compared with those of mock-infected counterparts.

With metal analysis data obtained using multiple complementary techniques, we further probed aspects of how *A. baumannii* infection altered iron metabolism in the host liver by analyzing the changes in gene expression of a selected panel of iron proteins in homogenized liver tissues. Specifically, we measured the mRNA levels of posttranscriptional regulators of iron proteins, IRP1 and IRP2; iron transporters, ferroportin-1 (FPN), transferrin receptor (TfR) and divalent metal transporter-1 (DMT1); the two subunits of the iron storage protein ferritin, ferritin heavy chain (FHC) and ferritin light chain (FLC); and two secreted factors associated with iron, hepcidin and lipocalin-2 (LCN2). Gene expression levels were normalized to the housekeeping gene, GAPDH, and additional housekeeping genes, HPRT1 and RLPL0, were measured to validate the use of GAPDH as the reference gene (Fig. 4*E*). Interestingly, a notable decrease in the mRNA of the iron exporter FPN was observed, consistent with a response to increased iron retention in this tissue. In contrast, the mRNA levels of hepcidin, a peptide hormone that regulates iron levels by degrading FPN, shows only moderate elevation at 24 h postinfection. Previous studies with infection models have shown hepcidin induction occurring during the first 12 h of infection (64), and the moderate change we observe is after the time window at which the hepcidin transcripts increase. The notable decrease in FPN mRNA suggests that hepatic iron regulation at this time point may also involve additional hepcidin-independent pathways that involve transcriptional regulation of FPN (65, 66). The mRNA levels of TfR appear unchanged while DMT1 mRNA levels are reduced in the infected mice compared with the mock-infected mice. We also found a significant reduction in serum transferrin during infection (*SI Appendix*, Fig. S16*A*). Transferrin has previously been shown to decrease during inflammation (67, 68). Both transferrin and DMT1 proteins are associated with the uptake of transferrin-bound iron. We also observe an increase in the mRNA levels of LCN2, a secreted glycoprotein that sequesters bacterial iron-binding siderophores to limit the bacterial growth (69) and has been implicated as an importer of both non–transferrin-bound iron (NTBI) and transferrin-bound iron (70, 71). Finally, we observe alteration in the gene expression of ferritin subunits, with up-regulation of FHC and down-regulation of FLC, which is consistent with modulation of the intracellular iron storage machinery (72). In particular, FHC has been shown to facilitate rapid iron uptake (72–74). Significant elevation in serum ferritin levels was also detected, with approximately 10-fold increase in ferritin abundance during infection (*SI Appendix*, Fig. S16*B*). This elevation corroborates previous studies that identified increased ferritin associated with LPS challenge and bacterial infections (67, 75). Consistent with alterations of ferritin levels is the decrease in the gene expression of the IRP proteins, IRP1 and IRP2, which have been shown to repress translation through binding to the iron responsive element on the ferritin mRNAs (76, 77). These qPCR data, combined with bioluminescence imaging of labile iron stores with ICL-1 and measurement of total iron levels by bulk and laser ablation ICP-MS, indicate that systemic *A. baumannii* infection alters the iron homeostasis of the host, manifested as elevated iron levels in the liver 24 h postinfection.

## Concluding Remarks

In summary, we have presented the design, synthesis, and characterization of ICL-1, a first-generation bioluminescence probe for in vivo imaging of labile iron stores in living animals, and its application to an *A. baumannii* infection model. ICL-1 utilizes a bioinspired $Fe^{2+}$-dependent endoperoxide cleavage reaction to release D-aminoluciferin and generate an increase in bioluminescent signal with high metal and oxidation state specificity. This probe is capable of monitoring changes in LIPs upon iron supplementation and/or depletion in live cells and animals, enabling the detection of dynamic alterations in $Fe^{2+}$ under physiological and pathological situations. Application of ICL-1 to an *A. baumannii* model of systemic infection showcases the utility of this probe for interrogating alterations in iron status in vivo, as we observe an increase in liver iron by direct ICP-MS and LA–ICP-MS data that is supported by complementary in vivo and ex vivo bioluminescent imaging using this probe. The combination of ICL-1 and related chemical probes with tissue-specific luciferase-expressing mice can increase spatial resolution. Consistent with the observed redistributions of hepatic iron and elevations in total hepatic iron, qPCR analyses of isolated liver tissues after infection reveal concomitant decreases in mRNA levels of the iron export protein ferroportin, increased mRNA levels of the secreted factor LCN2, and modulation in the mRNA levels of key iron storage machinery—namely, increased FHC and decreased FLC. These transcriptional changes are supported by significant alterations in serum transferrin and ferritin during infection. We hypothesize that such transcriptional alterations can serve as important contributors to changes in labile and total hepatic iron stores. By expanding our ability to monitor iron dynamics from cell culture to living animals, ICL-1 provides a unique chemical tool to study biological contributions of this essential metal nutrient and a starting point for developing next-generation probes for advancing our understanding of metals in biology in vivo.

## Materials and Methods

Full materials and procedures for the synthesis of compounds, spectroscopic characterization, and cellular imaging are described in *SI Appendix*. Primers used for real-time PCR analysis are shown in *SI Appendix*, Table S1. All animal studies were approved by and performed according to the guidelines of the Animal Care and Use Committee of the University of California, Berkeley and Vanderbilt University Medical Center. Experimental details of animal imaging experiments, infection models, and analysis of tissue and blood are described in *SI Appendix*.

**ACKNOWLEDGMENTS.** We thank Jessica Moore for technical assistance with tissue sectioning. We thank NIH [Grants GM79645 (to C.J.C.), AI101171 (to E.P.S.), AI105106 (to A.R.R.), and DK101293 (to A.S.)] for funding this work. C.J.C. is an Investigator with the Howard Hughes Medical Institute and a Canadian Institute for Advanced Research Senior Fellow. A.T.A. thanks the National Science Foundation for a graduate fellowship and was partially supported by NIH Chemical Biology Interface Training Grant T32 GM066698. M.C.H. thanks the University of California President's Postdoctoral Program for a fellowship. Z.R.L. is supported by the NIH Training Program in Environmental Toxicology (Grant T32 ES007028). B.S. acknowledges funding from an NIH Research Training Grant in Chemistry and Chemical Biology (Grant T32 GM064337).

1. Cammack R, Wrigglesworth JM, Baum H (1989) *Transport and Storage* (CRC, Boca Raton, FL).
2. Andrews NC (2000) Iron homeostasis: Insights from genetics and animal models. *Nat Rev Genet* 1:208–217.
3. Winterbourn CC (1995) Toxicity of iron and hydrogen peroxide: The Fenton reaction. *Toxicol Lett* 82-83:969–974.
4. Miller JL (2013) Iron deficiency anemia: A common and curable disease. *Cold Spring Harb Perspect Med* 3:a011866.
5. Torti SV, Torti FM (2013) Iron and cancer: More ore to be mined. *Nat Rev Cancer* 13:342–355.
6. Wu KJ, Polack A, Dalla-Favera R (1999) Coordinated regulation of iron-controlling genes, H-ferritin and IRP2, by c-MYC. *Science* 283:676–679.

7. Pinnix ZK, et al. (2010) Ferroportin and iron regulation in breast cancer progression and prognosis. *Sci Transl Med* 2:43ra56.
8. von Haehling S, Jankowska EA, van Veldhuisen DJ, Ponikowski P, Anker SD (2015) Iron deficiency and cardiovascular disease. *Nat Rev Cardiol* 12:659–669.
9. Hare D, Ayton S, Bush A, Lei P (2013) A delicate balance: Iron metabolism and diseases of the brain. *Front Aging Neurosci* 5:34.
10. James SA, et al. (2015) Direct in vivo imaging of ferrous iron dyshomeostasis in ageing *Caenorhabditis elegans*. *Chem Sci (Camb)* 6:2952–2962.
11. Skaar EP (2010) The battle for iron between bacterial pathogens and their vertebrate hosts. *PLoS Pathog* 6:e1000949.
12. Nairz M, Haschka D, Demetz E, Weiss G (2014) Iron at the interface of immunity and infection. *Front Pharmacol* 5:152.
13. Irving H, Williams RJP (1953) The stability of transition-metal complexes. *J Chem Soc* 1953:3192–3210.
14. Carter KP, Young AM, Palmer AE (2014) Fluorescent sensors for measuring metal ions in living systems. *Chem Rev* 114:4564–4601.
15. Aron AT, Loehr MO, Bogena J, Chang CJ (2016) An endoperoxide reactivity-based FRET probe for ratiometric fluorescence imaging of labile iron pools in living cells. *J Am Chem Soc* 138:14338–14346.
16. Au-Yeung HY, Chan J, Chantarojsiri T, Chang CJ (2013) Molecular imaging of labile iron(II) pools in living cells with a turn-on fluorescent probe. *J Am Chem Soc* 135: 15165–15173.
17. Spangler B, et al. (2016) A reactivity-based probe of the intracellular labile ferrous iron pool. *Nat Chem Biol* 12:680–685.
18. Hirayama T, Okuda K, Nagasawa H (2013) A highly selective turn-on fluorescent probe for iron(II) to visualize labile iron in living cells. *Chem Sci (Camb)* 4:1250–1256.
19. Niwa M, Hirayama T, Okuda K, Nagasawa H (2014) A new class of high-contrast Fe(II) selective fluorescent probes based on spirocyclized scaffolds for visualization of intracellular labile iron delivered by transferrin. *Org Biomol Chem* 12:6590–6597.
20. Hirayama T, et al. (2017) A universal fluorogenic switch for Fe(II) ion based on N-oxide chemistry permits the visualization of intracellular redox equilibrium shift towards labile iron in hypoxic tumor cells. *Chem Sci* 8:4858–4866.
21. Chan J, Dodani SC, Chang CJ (2012) Reaction-based small-molecule fluorescent probes for chemoselective bioimaging. *Nat Chem* 4:973–984.
22. Aron AT, Ramos-Torres KM, Cotruvo JA, Jr, Chang CJ (2015) Recognition- and reactivity-based fluorescent probes for studying transition metal signaling in living systems. *Acc Chem Res* 48:2434–2442.
23. Chen X, Tian X, Shin I, Yoon J (2011) Fluorescent and luminescent probes for detection of reactive oxygen and nitrogen species. *Chem Soc Rev* 40:4783–4804.
24. Yang Y, Zhao Q, Feng W, Li F (2013) Luminescent chemodosimeters for bioimaging. *Chem Rev* 113:192–270.
25. Cho DG, Sessler JL (2009) Modern reaction-based indicator systems. *Chem Soc Rev* 38: 1647–1662.
26. Dixon SJ, et al. (2012) Ferroptosis: An iron-dependent form of nonapoptotic cell death. *Cell* 149:1060–1072.
27. Dixon SJ, Stockwell BR (2014) The role of iron and reactive oxygen species in cell death. *Nat Chem Biol* 10:9–17.
28. Li J, Chen L, Du L, Li M (2013) Cage the firefly luciferin! A strategy for developing bioluminescent probes. *Chem Soc Rev* 42:662–676.
29. Xu T, et al. (2016) The expanding toolbox of in vivo bioluminescent imaging. *Front Oncol* 6:150.
30. Adams ST, Jr, Miller SC (2014) Beyond D-luciferin: Expanding the scope of bioluminescence imaging in vivo. *Curr Opin Chem Biol* 21:112–120.
31. Chen P, et al. (2017) Bioluminescent turn-on probe for sensing hypochlorite in vitro and in tumors. *Anal Chem* 89:5693–5696.
32. Takakura H, et al. (2015) New class of bioluminogenic probe based on bioluminescent enzyme-induced electron transfer: BioLeT. *J Am Chem Soc* 137:4010–4013.
33. Van de Bittner GC, Dubikovskaya EA, Bertozzi CR, Chang CJ (2010) In vivo imaging of hydrogen peroxide production in a murine tumor model with a chemoselective bioluminescent reporter. *Proc Natl Acad Sci USA* 107:21316–21321.
34. Van de Bittner GC, Bertozzi CR, Chang CJ (2013) Strategy for dual-analyte luciferin imaging: In vivo bioluminescence detection of hydrogen peroxide and caspase activity in a murine model of acute inflammation. *J Am Chem Soc* 135:1783–1795.
35. Godinat A, et al. (2013) A biocompatible in vivo ligation reaction and its application for noninvasive bioluminescent imaging of protease activity in living mice. *ACS Chem Biol* 8:987–999.
36. Chang YC, Chao PW, Tung CH (2011) Sensitive luciferin derived probes for selective carboxypeptidase activity. *Bioorg Med Chem Lett* 21:3931–3934.
37. Dragulescu-Andrasi A, Liang G, Rao J (2009) In vivo bioluminescence imaging of furin activity in breast cancer cells using bioluminogenic substrates. *Bioconjug Chem* 20: 1660–1666.
38. Eiríksdóttir E, Mäger I, Lehto T, El Andaloussi S, Langel U (2010) Cellular internalization kinetics of (luciferin-)cell-penetrating peptide conjugates. *Bioconjug Chem* 21:1662–1672.
39. Henkin AH, et al. (2012) Real-time noninvasive imaging of fatty acid uptake in vivo. *ACS Chem Biol* 7:1884–1891.
40. Jones LR, et al. (2006) Releasable luciferin-transporter conjugates: Tools for the real-time analysis of cellular uptake and release. *J Am Chem Soc* 128:6526–6527.
41. Mofford DM, Adams STJ, Jr, Reddy GS, Reddy GR, Miller SC (2015) Luciferin amides enable in vivo bioluminescence detection of endogenous fatty acid amide hydrolase activity. *J Am Chem Soc* 137:8684–8687.
42. Porterfield WB, Jones KA, McCutcheon DC, Prescher JA (2015) A "caged" luciferin for imaging cell-cell contacts. *J Am Chem Soc* 137:8656–8659.
43. Rush JS, Beatty KE, Bertozzi CR (2010) Bioluminescent probes of sulfatase activity. *ChemBioChem* 11:2096–2099.
44. Vorobyeva AG, et al. (2015) Development of a bioluminescent nitroreductase probe for preclinical imaging. *PLoS One* 10:e0131037.
45. Yao H, So MK, Rao J (2007) A bioluminogenic substrate for in vivo imaging of beta-lactamase activity. *Angew Chem Int Ed Engl* 46:7031–7034.
46. Zhou W, et al. (2008) Self-cleavable bioluminogenic luciferin phosphates as alkaline phosphatase reporters. *ChemBioChem* 9:714–718.
47. Cohen AS, Dubikovskaya EA, Rush JS, Bertozzi CR (2010) Real-time bioluminescence imaging of glycans on live cells. *J Am Chem Soc* 132:8563–8565.
48. Sellmyer MA, et al. (2013) Visualizing cellular interactions with a generalized proximity reporter. *Proc Natl Acad Sci USA* 110:8567–8572.
49. Heffern MC, et al. (2016) In vivo bioluminescence imaging reveals copper deficiency in a murine model of nonalcoholic fatty liver disease. *Proc Natl Acad Sci USA* 113: 14219–14224.
50. Spangler B, et al. (2016) A novel tumor-activated prodrug strategy targeting ferrous iron is effective in multiple preclinical cancer models. *J Med Chem* 59:11161–11170.
51. Fontaine SD, DiPasquale AG, Renslo AR (2014) Efficient and stereocontrolled synthesis of 1,2,4-trioxolanes useful for ferrous iron-dependent drug delivery. *Org Lett* 16: 5776–5779.
52. Tang Y, et al. (2005) Dispiro-1,2,4-trioxane analogues of a prototype dispiro-1,2,4-trioxolane: Mechanistic comparators for artemisinin in the context of reaction pathways with iron(II). *J Org Chem* 70:5103–5110.
53. Creek DJ, et al. (2007) Iron-mediated degradation kinetics of substituted dispiro-1,2,4-trioxolane antimalarials. *J Pharm Sci* 96:2945–2956.
54. Lauterwasser EM, et al. (2015) Trioxolane-mediated delivery of mefloquine limits brain exposure in a mouse model of malaria. *ACS Med Chem Lett* 6:1145–1149.
55. Cerchiaro G, Manieri TM, Bertuchi FR (2013) Analytical methods for copper, zinc and iron quantification in mammalian cells. *Metallomics* 5:1336–1345.
56. Epsztejn S, Kakhlon O, Glickstein H, Breuer W, Cabantchik I (1997) Fluorescence analysis of the labile iron pool of mammalian cells. *Anal Biochem* 248:31–40.
57. Rubino JT, Franz KJ (2012) Coordination chemistry of copper proteins: How nature handles a toxic cargo for essential function. *J Inorg Biochem* 107:129–143.
58. Cotruvo JA, Jr, Aron AT, Ramos-Torres KM, Chang CJ (2015) Synthetic fluorescent probes for studying copper in biological systems. *Chem Soc Rev* 44:4400–4414.
59. Ramos-Torres KM, Kolemen S, Chang CJ (2016) Thioether coordination chemistry for molecular imaging of copper in biological systems. *Isr J Chem* 56:724–737.
60. Ackerman CM, Lee S, Chang CJ (2017) Analytical methods for imaging metals in biology: From transition metal metabolism to transition metal signaling. *Anal Chem* 89: 22–41.
61. Hahn P, et al. (2009) Age-dependent and gender-specific changes in mouse tissue iron by strain. *Exp Gerontol* 44:594–600.
62. Kong WN, et al. (2014) Sex differences in iron status and hepcidin expression in rats. *Biol Trace Elem Res* 160:258–267.
63. Palmer LD, Skaar EP (2016) Transition metals and virulence in bacteria. *Annu Rev Genet* 50:67–91.
64. Arezes J, et al. (2015) Hepcidin-induced hypoferremia is a critical host defense mechanism against the siderophilic bacterium *Vibrio vulnificus*. *Cell Host Microbe* 17: 47–57.
65. Guida C, et al. (2015) A novel inflammatory pathway mediating rapid hepcidin-independent hypoferremia. *Blood* 125:2265–2275.
66. Enculescu M, et al. (2017) Modelling systemic iron regulation during dietary iron overload and acute inflammation: Role of hepcidin-independent mechanisms. *PLoS Comput Biol* 13:e1005322.
67. Neves JV, Wilson JM, Rodrigues PN (2009) Transferrin and ferritin response to bacterial infection: The role of the liver and brain in fish. *Dev Comp Immunol* 33:848–857.
68. Ritchie RF, et al. (1999) Reference distributions for the negative acute-phase serum proteins, albumin, transferrin and transthyretin: A practical, simple and clinically relevant approach in a large cohort. *J Clin Lab Anal* 13:273–279.
69. Goetz DH, et al. (2002) The neutrophil lipocalin NGAL is a bacteriostatic agent that interferes with siderophore-mediated iron acquisition. *Mol Cell* 10:1033–1043.
70. Bao G, et al. (2010) Iron traffics in circulation bound to a siderocalin (Ngal)-catechol complex. *Nat Chem Biol* 6:602–609.
71. Correnti C, Strong RK (2012) Mammalian siderophores, siderophore-binding lipocalins, and the labile iron pool. *J Biol Chem* 287:13524–13531.
72. Pham CG, et al. (2004) Ferritin heavy chain upregulation by NF-kappaB inhibits TNFalpha-induced apoptosis by suppressing reactive oxygen species. *Cell* 119: 529–542.
73. Torti SV, Torti FM (1994) Iron and ferritin in inflammation and cancer. *Adv Inorg Biochem* 10:119–137.
74. Rucker P, Torti FM, Torti SV (1996) Role of H and L subunits in mouse ferritin. *J Biol Chem* 271:33352–33357.
75. Carraway MS, Ghio AJ, Taylor JL, Piantadosi CA (1998) Induction of ferritin and heme oxygenase-1 by endotoxin in the lung. *Am J Physiol* 275:L583–L592.
76. Muckenthaler MU, Galy B, Hentze MW (2008) Systemic iron homeostasis and the iron-responsive element/iron-regulatory protein (IRE/IRP) regulatory network. *Annu Rev Nutr* 28:197–213.
77. Rouault TA (2006) The role of iron regulatory proteins in mammalian iron homeostasis and disease. *Nat Chem Biol* 2:406–414.